

Near-threshold photoelectron holography beyond the strong-field approximation

XuanYang Lai¹, ShaoGang Yu^{1,2}, YiYi Huang^{1,2}, LinQiang Hua¹, Cheng Gong¹, Wei Quan¹, C. Figueira de Morisson Faria^{3,*} and XiaoJun Liu^{1†}

¹State Key Laboratory of Magnetic Resonance and Atomic and Molecular Physics and Center for Cold Atom Physics, Wuhan Institute of Physics and Mathematics, Chinese Academy of Sciences, Wuhan 430071, China

²School of Physics, University of Chinese Academy of Sciences, Beijing 100080, China

³Department of Physics and Astronomy, University College London, Gower Street, London WC1E 6BT, United Kingdom

(Dated: July 10, 2018)

We study photoelectron angular distributions (PADs) near the ionization threshold with a newly developed Coulomb quantum-orbit strong-field approximation (CQSFA) theory. The CQSFA simulations present an excellent agreement with the result from time-dependent Schrödinger equation method. We show that the low-energy fan-shaped structure in the PADs corresponds to a subcycle time-resolved holographic structure and stems from the significant influence of the Coulomb potential on the phase of the forward-scattering electron trajectories, which affects different momenta and scattering angles unequally. For the first time, our work provides a direct explanation of how the fan-shaped structure is formed, based on the quantum interference of direct and forward-scattered orbits.

PACS numbers: 32.80.Rm, 32.80.Qk, 42.50.Hz

Quantum interference of matter waves lies at the heart of quantum mechanics. When an atom or a molecule interacts with a strong laser field, the bound electron may be ionized by tunneling through the barrier formed by the Coulomb potential and the laser electric field [1]. The electron wavepackets ionized at different times with the same final momentum will interfere with each other [2]. This results in rich interference patterns in the above-threshold ionization (ATI) photoelectron angular distributions (PADs) [3], which have been taken as an important tool in exploring the structure and the dynamics of atoms and molecules with attosecond temporal resolution and angstrom spatial resolution [4, 5].

Recently, a new type of wavepacket interference, i.e., photoelectron holography [6–9], has provided a novel avenue for ultrafast studies of structural and dynamical information about the atomic or molecular medium. By analogy with optical holography [10], the electron wavepacket which directly drifts to the detector after tunneling ionization is taken as reference wave, while the electron wavepacket which further interacts with the core and then drifts to the detector acts as signal wave. These two paths with the same final momentum interfere with each other, forming the holographic patterns in the PADs. Since the signal wave scatters off the target and encodes its structure, the hologram stores spatial and temporal information about the core- and electron dynamics. For example, a “fork”-like holographic structure was experimentally observed in the PADs of metastable xenon atoms [6, 7]. This specific structure is produced by the direct and the laser-driven forward-scattering electron wavepackets from the same quarter cycle of the laser pulse; thus, subcycle time resolution is

encoded in the holographic patterns [6, 7]. Furthermore, signal and reference waves can be born in different quarter cycles, leading to different holographic structures [11–14]. For instance, a fishbone-like holographic structure from the interference by the direct and the backscattered electron wavepackets has been identified experimentally [15]. This structure has been proposed as a particularly sensitive probe of the molecular structures [12]. Hence, how to decode the structural and dynamical information about the target from a given holographic structure has also attracted great attention. This has led to a novel approach for extracting the phase of the scattering amplitude of the signal wave, providing time-resolved imaging of ultrafast processes [16].

Nonetheless, the understanding of time-resolved photoelectron holography is still quite preliminary. Holographic patterns are usually understood within the strong-field approximation (SFA) [1, 2], or semiclassical models in which the influence of the ionic Coulomb potential on the dynamics of the ionized electron is fully neglected [11, 12]. Recently, however, the Coulomb potential has been found to play an important role in the photoelectron spectra, leading to, e.g., an unexpected low-energy structure [17–21] and even a zero-energy structure [22, 23]. The Coulomb potential also modifies the holographic patterns, resulting in, e.g., the reduced fringe spacing in the “fork”-like holographic structure [6, 7] and the appearance of the clear backscattering holography due to the Coulomb focusing [11–13]. The physics behind the Coulomb effects is however poorly understood, which greatly hinders a comprehensive understanding of photoelectron holography and its potential applications in strong field and attosecond physics.

Another structure caused by the interplay between the Coulomb potential and the laser field is a fan-shaped interference pattern that appears in two-dimensional PADs near the ionization threshold. This structure has been measured in several experiments [6, 24, 25] and has been

*Electronic address: c.faria@ucl.ac.uk

†Electronic address: xjliu@wipm.ac.cn

the topic of theoretical studies since the past decade [26–29]. Regardless, there is no direct explanation of how this pattern forms. Empirical rules for predicting the number of fringes have been given in [26, 28], but this rule loses its efficacy as the laser intensity is increased [30]. Furthermore, in [26] the patterns were related to laser-dressed Kepler hyperbolae with neighboring angular momenta. However, the arguments in [26] are backed by classical-trajectory Monte-Carlo computations, for which quantum interference is absent. This means that there is no direct evidence that the fanlike structure can be reproduced, or of how it develops. Subsequently, the fan-shaped structure is reproduced with Coulomb-Volkov approximation [27], for which the influence of the Coulomb potential is included in the final electron state, but not in the continuum propagation. Hence, it does not provide information on how the Coulomb potential changes the electron trajectories and only allows a vague explanation for how the patterns form. Therefore, a new theoretical method is required to reveal the underlying physics of the Coulomb effect on the fan-shaped interference patterns.

In this paper, we study the above-mentioned fan-shaped structure with a Coulomb quantum-orbit strong-field approximation (CQSFA) theory [31]. This newly developed approach exhibits a very good agreement with the result from the time-dependent Schrödinger equation (TDSE), and allows a direct assessment of quantum interference in terms of a few electron trajectories and their phase differences. We perform a detailed analysis of how the fan-shaped pattern forms, and, more importantly, show that it corresponds to a subcycle time-resolved holographic structure arising from the interference between the direct and the forward-scattered electron wavepackets. This type of forward scattering is absent in the SFA, and corresponds to trajectories along which the electron is deflected by the Coulomb potential without undergoing a hard collision with the core. Due to the Coulomb potential, the phase associated with the forward-scattering trajectories is significantly changed. These distortions are angle dependent, and more dramatic for lower-energy photoelectrons, resulting in the specific fan-shaped structure. Thus, our work for the first time explains the underlying physics of the Coulomb effect on the fan-shaped structure. Additionally, we analyze the electron ionization dynamics and identify a clear signature of nonadiabatic tunneling.

The CQSFA theory [31] employed in this work describes ionization in terms of quantum orbits from the saddle-point evaluation of the ionization amplitude. Conceptually, it differs from the Coulomb-corrected SFA (CCSFA) theory [32, 33] and the Eikonal Volkov approximation (EVA) [34], which are the most widespread Coulomb-corrected strong-field approaches. While the EVA is derived from a laser-dressed Wentzel-Kramers-Brillouin (WKB) approach in the limit of small scattering angles, and the CCSFA constructs its trajectories recursively starting from the Coulomb-free trajectories used in the SFA, the CQSFA is derived using path-integral methods, which are applied to the full time-evolution operator.

From the implementation viewpoint, there are also differences as the CCSFA solves the direct problem of seeking the final momentum for a given initial momentum, while the CQSFA focuses on the inverse problem. An important consequence is that sampling in the CCSFA is implemented to obtain a large number of orbits and then these trajectories are binned according to their final momenta. Thus, in practice, there is a huge amount of electron trajectories in the CCSFA, while, in the CQSFA, a few electron trajectories suffice. For example, for each photoelectron in the low-energy region, three trajectories within a driving-field cycle are needed for obtaining converged PADs. Therefore, by analyzing the phase difference between these few orbits, we can directly understand how the interference patterns are formed and how the Coulomb potential influences this interference.

Briefly, in the CQSFA theory, the initial state is a bound state $|\psi_0(t_0)\rangle = e^{iI_p t_0} |\psi_0\rangle$, and the final state is a continuum state $|\psi_{\mathbf{p}_f}(t)\rangle$ with momentum \mathbf{p}_f . This gives the ionization amplitude (in atomic units) [2]

$$M(\mathbf{p}_f) = -i \lim_{t \rightarrow \infty} \int_{-\infty}^t dt_0 \langle \psi_{\mathbf{p}_f}(t) | \hat{U}(t, t_0) \hat{H}_I(t_0) | \psi_0(t_0) \rangle, \quad (1)$$

where $\hat{U}(t, t_0)$ is the time-evolution operator of the Hamiltonian $\hat{H}(t) = \hat{\mathbf{p}}^2/2 + V(\hat{\mathbf{r}}) + \hat{H}_I(t)$ with $\hat{H}_I(t) = -\hat{\mathbf{r}} \cdot \mathbf{E}(t)$. Note that Eq. (1) is formally exact. Employing the Feynman path-integral formalism [35, 36] and the saddle-point approximation [37, 38], Eq. (1) becomes

$$M(\mathbf{p}_f) \propto -i \lim_{t \rightarrow \infty} \sum_s \left\{ \det \left[\frac{\partial \mathbf{p}_s(t)}{\partial \mathbf{r}_s(t_0, s)} \right] \right\}^{-1/2} e^{iS(\bar{\mathbf{p}}_s, \mathbf{r}_s, t_0, s, t)} \times \mathcal{C}(t_0, s) \langle \mathbf{p}_s(t_0, s) + \mathbf{A}(t_0, s) | \hat{H}_I(t_0, s) | \psi_0 \rangle, \quad (2)$$

where the term $\mathcal{C}(t_0)$ is the prefactor, $\partial \mathbf{p}(t)/\partial \mathbf{r}(t_0)$ is related to the stability of the trajectory, $S(\bar{\mathbf{p}}, \mathbf{r}, t_0, t) = I_p t_0 - \int_{t_0}^t d\tau [\dot{\mathbf{p}} \cdot \mathbf{r}(\tau) + \bar{\mathbf{p}}^2/2 + V(\mathbf{r})]$ denotes the action, in which the term $\dot{\mathbf{p}} \cdot \mathbf{r}(\tau)$ is important for obtaining correct interference patterns [39], I_p is the ionization potential, \mathbf{p} is the field-dressed momentum and $\bar{\mathbf{p}} = \mathbf{p} + \mathbf{A}(\tau)$, with $t_0 < \tau < t$, is the electron velocity. The index s denotes the different orbits from three saddle-point equations: $[\mathbf{p}_0 + \mathbf{A}(t_0)]^2/2 + I_p = 0$, $\dot{\mathbf{p}}(\tau) = -\nabla_{\mathbf{r}} V[\mathbf{r}(\tau)]$ and $\dot{\mathbf{r}}(\tau) = \mathbf{p}(\tau) + \mathbf{A}(\tau)$, which are solved using an iteration scheme for any given final momentum [31] with the assumption that the electron is ionized by tunneling from t_0 to $t_0^R = \text{Re}[t_0]$ and then moves to the detector with the real time [40, 41] (see the supplemental material).

Figs. 1(a) and (b) exhibit the two-dimensional PADs near the ionization threshold computed for the hydrogen atom in a linearly polarized laser field with the CQSFA and the SFA, respectively. As a benchmark, we take the *ab initio* TDSE calculation shown in Fig. 1(c), which is solved using the freely available software Qprop [42]. Our results show significant changes in the PAD for the CQSFA, in comparison with the SFA simulation. Indeed, there are eight clear peaks in the first ATI ring at the momentum $p_f \sim 0.2$ a.u. [29], while only four peaks are

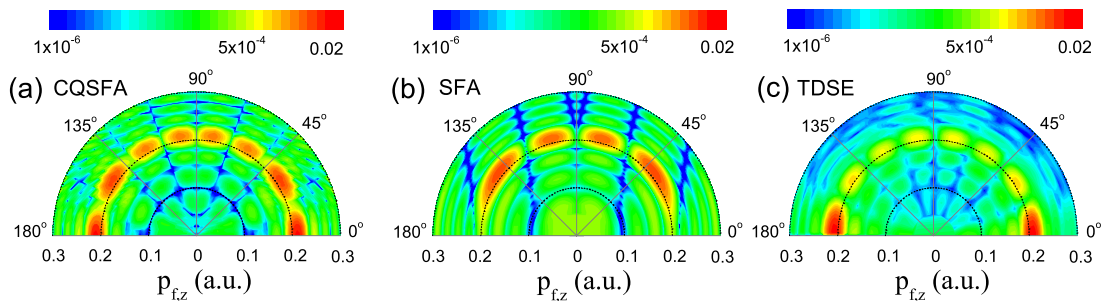


FIG. 1: (Color online) Two-dimensional PADs of hydrogen atom ($I_p = 0.5$ a.u.) near the ionization threshold in a linearly polarized laser field of intensity $I = 2 \times 10^{14}$ W/cm² and wavelength $\lambda = 800$ nm, for momenta $p_f < 0.3$ a.u. Panels (a), (b) and (c) refer to CQSFA, SFA, and TDSE, respectively. The momentum component along the laser polarization direction is given by $p_{f,z}$. In panels (a) and (b), we have used $\mathbf{E}(t) = \hat{\mathbf{z}}E_0 \sin \omega t$ over five cycles, while in panel (c) we have taken a long laser pulse $\mathbf{E}(t) = \hat{\mathbf{z}}E_0 \sin \omega t \times f(t)$ with a trapezoidal profile $f(t)$ (up and down-ramped over 2 cycles, constant over 8 cycles). The TDSE spectra have been computed employing a window operator of width 5×10^{-4} a.u. as discussed in [42]. All panels have been normalized to the same range to facilitate a direct comparison.

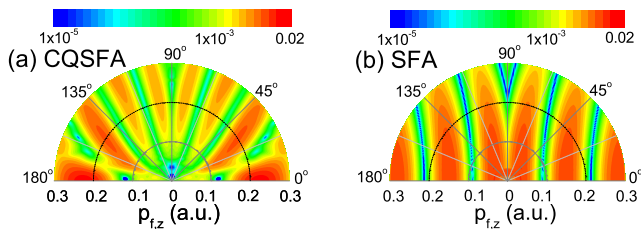


FIG. 2: (Color online) Same as Figs. 1(a) and (b), but calculated with quantum orbits occurred in one optical cycle.

found in the corresponding SFA simulations. Note that the number of the peaks will be changed for other initial states of atom and laser parameters; for more details, see the supplemental material. Moreover, in Fig. 1(a) a clear radial fanlike pattern is present between the threshold region and the onset of the ATI ring, which completely disappears in Fig. 1(b). The overall interference pattern in CQSFA exhibits a very good agreement with the TDSE simulations in Fig. 1(c), reflecting the significant role of the Coulomb potential on strong-field ionization, which is consistent with previous publications [26, 27]. There is however a slight quantitative discrepancy between CQSFA and TDSE in the amplitudes of the eight peaks. Possible reasons are provided in the supplemental material. In this work, however, we focus on how the Coulomb potential leads to the generation of the fanlike structure by analyzing quantum orbits from the CQSFA.

In Fig. 2 we consider only the interference of the orbits within one driving-field cycle, i.e., the intracycle interference [29]. The CQSFA outcome [Fig. 2(a)] exhibits eight interference stripes, which, near the ionization threshold, roughly point to zero momentum, showing a divergent structure. In contrast, for the SFA simulations in Fig. 2(b), there are only six approximately vertical interference stripes, which bend as the transverse momentum increases. If quantum-orbit contributions from other optical cycles are also added coherently, intercycle interference [29] forms characteristic ATI rings centered around

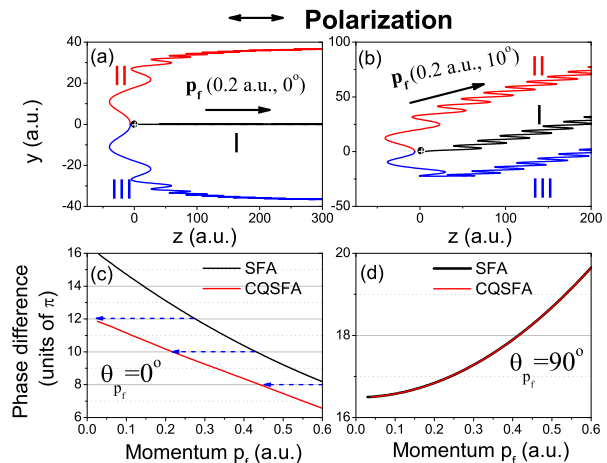


FIG. 3: (Color online) (a) and (b) Illustration of three orbits from the CQSFA theory in the yz plane for electrons with fixed final momentum $p_f = 0.2$ a.u. along the 0° and 10° directions with respect to the laser polarization, respectively. The laser polarization is along the z axis. The black circle at the position $(0,0)$ denotes the nucleus. (c) and (d) Phase difference between orbits I and II as a function of p_f along 0° and 90° directions with respect to the laser polarization, respectively. The blue arrows denote the shift of the positions of the interference maxima.

zero momentum. The modulation between the intracycle and intercycle interferences results in the clear eight peaks in the first ATI ring in CQSFA and the four ATI peaks in SFA, just as illustrated in Figs. 1(a) and (b), respectively. Moreover, the divergent structure in Fig. 2(a) corresponds to the fanlike pattern shown in the PADs. Thus, the difference between Figs. 1(a) and (b) stems from the influence of the Coulomb potential on the intracycle interference.

More insight can be gained by analyzing the positions of the interference stripes in the PADs. In the CQSFA theory, the amplitude of the intracycle interference in the low-energy region is mainly determined by three quan-

tum orbits [31]. Figs. 3(a) and (b) depict these orbits in the yz plane for electrons with fixed final momentum $p_f = 0.2$ a.u. along the 0° and 10° directions with respect to the laser polarization, respectively. For orbit I, the electron moves directly towards the detector without returning to the parent ion. In contrast, for orbits II and III, the electron will turn around the core and then move to the detector along Kepler hyperbolae to which a quiver motion caused by the laser field is superimposed [26, 32]. Therefore, the patterns in Fig. 2(a) correspond to a holographic structure from the interference between the direct trajectories and forward-scattering trajectories, which are deflected by the core but do not undergo hard collisions. Orbits I and II are similar to the so-called short and long trajectories in SFA [11], while orbit III is not found in the SFA and is observed after the Coulomb potential is considered [6, 32]. If the final momentum is along the laser polarization [Fig. 3(a)], orbits II and III are symmetric with respect to the polarization direction. With increasing scattering angle $\theta_{\mathbf{p}_f}$, orbit III will experience a stronger attraction from the Coulomb potential, leading to a larger deflection [see, e.g., Fig. 3(b)]. Due to Coulomb defocusing, the amplitude of orbit III decreases significantly with increasing scattering angle, while the contributions from orbits I and II become dominant. This results in well defined reference and probe signals in the holographic patterns: orbits I and II, respectively.

Hence, we will focus on the phase difference between orbits I and II, $\Delta\Phi = \Phi_I - \Phi_{II}$, which is directly related to the interference pattern and is displayed in Figs. 3(c) and (d) as a function of the final electron momentum, for parallel and perpendicular scattering angles, respectively. A similar analysis has been employed in our previous publications [31, 43]. For $\theta_{\mathbf{p}_f} = 0^\circ$, the phase difference decreases if the Coulomb potential is incorporated. This shifts the interference maxima in the CQSFA spectra towards lower energies, in comparison with their SFA counterparts (see the blue dashed arrows). Physically, this happens because, in comparison with orbit I, orbit II accumulates a larger positive phase contribution from the Coulomb potential as it passes by the core, $-\int_{t'}^t V[\mathbf{r}(\tau)]d\tau$ [see Eq. (2)]. With increasing $\theta_{\mathbf{p}_f}$, the above-mentioned shift becomes smaller and is almost negligible for perpendicular emission [Fig. 3(d)]. This is not surprising since for $\theta_{\mathbf{p}_f} = 90^\circ$ orbits I and II are symmetric with respect to the y axis. Thus, the influence of the Coulomb potential on the two orbits is the same. A similar result has been reported in the study of the interference carpets in ATI [44]. Therefore, more interference stripes will appear in the low-energy region for the CQSFA, in agreement with Fig. 2(a). Furthermore, the shift in $\Delta\Phi$ is more significant for smaller momenta [Fig. 3(c)] as, in this case, the electron will need a longer time to leave the core region. This will result in a larger positive phase contribution from the Coulomb potential and a larger decrease in $\Delta\Phi$. Therefore, the interference maxima in the photoelectron spectra will shift more dramatically for smaller momenta. A similar behavior is observed for other emission angles $\theta_{\mathbf{p}_f}$, leading to the

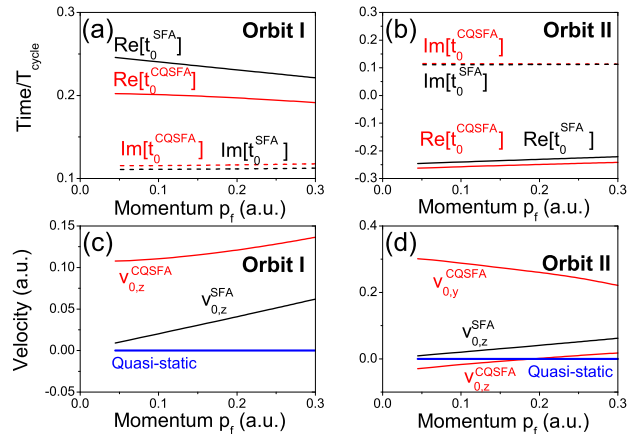


FIG. 4: (Color online) (a) and (b) The real part (solid lines) and imaginary part (dashed lines) of the tunneling time for electrons with $\theta_{\mathbf{p}_f} = 0^\circ$ in CQSFA (red) and in SFA (black). (c) and (d) The corresponding initial velocity at the tunneling exit. The quasi-static expected velocity is denoted by the blue lines. (a)(c): orbit I and (b)(d): orbit II.

fanlike structures in Figs. 1(a) and 2(a).

Finally, Figs. 4(a) and (b) show the tunneling time of the photoelectrons from CQSFA and SFA for orbits I and II, respectively, for a specific angle $\theta_{\mathbf{p}_f} = 0^\circ$. Due to the ionization by tunneling, the time t_0 becomes complex [2], and $\text{Im}[t_0] > 0$ can be related to the tunneling time through the potential barrier. For each kind of orbit, the photoelectrons are initially ionized within a temporal window of about $0.02T_{\text{cycle}}$ (~ 60 attoseconds), and the orbits I and II originate from the adjacent quarter cycles of the laser pulse. Therefore, the subcycle fan-shaped structure has recorded attosecond time-resolved electronic dynamics. In comparison with the SFA, for a given final momentum \mathbf{p}_f , $\text{Re}(t_0)$ in the CQSFA approaches the driving-field crossing ($t = 0$) or its crest ($t = -0.25T_{\text{cycle}}$) for orbit I or II, respectively. This increases (decreases) the initial field-dressed momentum \mathbf{p}_0 for orbit I (orbit II). Along orbit I, the electron compensates the deceleration in the Coulomb potential as it moves towards the detector, while, for orbit II, the electron is accelerated significantly along the polarization direction due to the interplay of the Coulomb potential and the laser field [31, 40]. In Figs. 4(c) and (d) we illustrate the change in the initial velocity $\mathbf{v}_0 = \mathbf{p}_0 + \mathbf{A}(\text{Re}[t_0])$ at the tunneling exit. Both CQSFA and SFA simulations significantly deviate from the adiabatic tunneling theory (blue lines in Fig. 4), in which the electron is assumed to begin its journey in the continuum with vanishing velocity [1, 45, 46].

In summary, we have performed a detailed analysis of the low-energy fanlike structure observed in PADs using a CQSFA theory, in which only a few electron trajectories are required to describe strong-field ionization, and which poses no restriction upon the scattering angle. We show that this structure constitutes a subcycle time-resolved

holographic pattern from the interference of direct electron trajectories and forward-scattered trajectories that are deflected, but do not undergo hard collisions with the core. We go beyond existing studies by providing direct and in-depth evidence of how the Coulomb potential alters the phase of the forward-scattering trajectories, which affects different scattering angles and electron momenta unequally, leading to the above-mentioned fanlike structure. The present method can be applied to the

understanding of Coulomb effects on other holographic patterns, e.g., the well-known reduced fringe spacing in the “fork”-like holographic structure [6, 7].

We thank Prof. Wilhelm Becker and Prof. Xue-Bin Bian for many useful discussions. This work is supported by the National Basic Research Program of China Grant (No. 2013CB922201), the NNSF of China (Nos. 11374329, 11334009, 11474321, and 11527807) and the UK EPSRC (No. EP/J019240/1).

-
- [1] L. V. Keldysh, Zh. Eksp. Teor. Fiz. **47**, 1945 (1964) [Sov. Phys. JETP **20**, 1307 (1965)]; F. H. M. Faisal, J. Phys. B **6**, L89 (1973); H. R. Reiss, Phys. Rev. A **22**, 1786 (1980).
- [2] W. Becker, F. Grasbon, R. Kopold, D. B. Milošević, G. G. Paulus and H. Walther, Adv. At. Mol. Opt. Phys. **48**, 35 (2002).
- [3] F. Lindner *et al.*, Phys. Rev. Lett. **95**, 040401 (2005).
- [4] M. Meckel, A. Staudte, S. Patchkovskii, D. M. Villeneuve, P. B. Corkum, R. Dörner, and M. Spanner, Nat. Phys. **10**, 594 (2014).
- [5] X. H. Xie, Phys. Rev. Lett. **114**, 173003 (2015).
- [6] Y. Huismans *et al.*, Science **331**, 61 (2010).
- [7] Y. Huismans *et al.*, Phys. Rev. Lett. **109**, 013002 (2012).
- [8] M. Meckel *et al.*, Science **320**, 1478 (2008).
- [9] M. Li, X. Sun, X. Xie, Y. Shao, Y. Deng, C. Wu, Q. Gong, and Y. Liu, Sci. Rep. **5**, 8519 (2015).
- [10] D. Gabor, Nature (London) **161**, 777 (1948).
- [11] X.-B. Bian *et al.*, Phys. Rev. A **84**, 043420 (2011).
- [12] X.-B. Bian and A. D. Bandrauk, Phys. Rev. Lett. **108**, 263003 (2012).
- [13] X.-B. Bian and A. D. Bandrauk, Phys. Rev. A **89**, 033423 (2014).
- [14] Daniel D. Hickstein *et al.*, Phys. Rev. Lett. **109**, 073004 (2012).
- [15] M. Haertelt, X.-B. Bian, M. Spanner, A. Staudte, and P. B. Corkum, Phys. Rev. Lett. **116**, 133001 (2016).
- [16] Y. M. Zhou, O. I. Tolstikhin, and T. Morishita, Phys. Rev. Lett. **116**, 173001 (2016).
- [17] C. I. Blaga, F. Catoire, P. Colosimo, G. G. Paulus, H. G. Muller, P. Agostini, and L. F. Dimauuro, Nat. Phys. **5**, 335 (2009).
- [18] W. Quan *et al.*, Phys. Rev. Lett. **103**, 093001 (2009).
- [19] W. Becker *et al.*, J. Phys. B **47**, 204022 (2014).
- [20] C. Y. Wu *et al.*, Phys. Rev. Lett. **109**, 043001 (2012).
- [21] W. Becker and D. B. Milošević, J. Phys. B **48**, 151001 (2015).
- [22] J. Dura *et al.*, Sci. Rep. **3**, 2675 (2013).
- [23] W. Quan *et al.*, Sci. Rep. **6**, 27108 (2016).
- [24] A. Rudenko *et al.*, J. Phys. B **37**, L407 (2004).
- [25] C. M. Maharjan *et al.*, J. Phys. B **39**, 1955 (2004).
- [26] D. G. Arbó *et al.*, Phys. Rev. Lett. **96**, 143003 (2006); D. G. Arbó *et al.*, Phys. Rev. A **78**, 013406 (2008).
- [27] D. G. Arbó *et al.*, Phys. Rev. A **77**, 013401 (2008).
- [28] Z. Chen *et al.*, Phys. Rev. A **74**, 053405 (2006).
- [29] D. G. Arbó *et al.*, Phys. Rev. A **81**, 021403(R) (2010); D. G. Arbó *et al.*, Nucl. Instrum. Methods B **279**, 24 (2012).
- [30] T. Marchenko, H. G. Muller, K. J. Schafer and M. J. J. Vrakking, J. Phys. B **43**, 095601 (2010).
- [31] X. Y. Lai, C. Poli, H. Schomerus, and C. Figueira de Morisson Faria, Phys. Rev. A **92**, 043407 (2015).
- [32] T. M. Yan, S. V. Popruzhenko, M. J. J. Vrakking, and D. Bauer, Phys. Rev. Lett. **105**, 253002 (2010).
- [33] T. M. Yan and D. Bauer, Phys. Rev. A **86**, 053403 (2012).
- [34] O. Smirnova, M. Spanner, and M. Ivanov, Phys. Rev. A **77**, 033407 (2008).
- [35] H. Kleinert, *Path integrals in quantum mechanics, statistics, polymer physics, and financial markets*, (World Scientific, 2009).
- [36] D. B. Milošević, J. Math. Phys. **54**, 042101(2013).
- [37] C. Figueira de Morisson Faria, H. Schomerus, and W. Becker, Phys. Rev. A **66**, 043413 (2002).
- [38] R. Kopold, W. Becker, and M. Kleber, Opt. Commun. **179**, 39 (2000).
- [39] N. I. Shvetsov-Shilovski *et al.*, Phys. Rev. A **94**, 013415 (2016).
- [40] S. V. Popruzhenko and D. Bauer, J. Mod. Opt. **55**, 2573 (2008).
- [41] S. V. Popruzhenko, J. Phys. B **47**, 204001 (2014).
- [42] D. Bauer and P. Koval, Comput. Phys. Commun. **174**, 396 (2006); see also www.qprop.de.
- [43] X. Y. Lai and C. Figueira de Morisson Faria, Phys. Rev. A **88**, 013406 (2013).
- [44] Ph. A. Korneev *et al.*, Phys. Rev. Lett. **108**, 223601 (2012).
- [45] O. Pedatzur *et al.*, Nat. Phys. **11**, 815 (2015).
- [46] M. Y. Ivanov, M. Spanner, and O. Smirnova, J. Mod. Opt. **52**, 165 (2005).